Tank-Treading of Erythrocytes in Strong Shear Flows via a Nonstiff Cytoskeleton-Based Continuum Computational Modeling

W. R. Dodson III[†] and P. Dimitrakopoulos[‡*]
[†]Fischell Department of Bioengineering and [‡]Department of Chemical and Biomolecular Engineering, University of Maryland, College Park, Maryland

ABSTRACT We develop a computationally efficient cytoskeleton-based continuum erythrocyte algorithm. The cytoskeleton is modeled as a two-dimensional elastic solid with comparable shearing and area-dilatation resistance that follows a material law (Skalak, R., A. Tozeren, R. P. Zarda, and S. Chien. 1973. Strain energy function of red blood cell membranes. *Biophys. J.* 13:245–264). Our modeling enforces the global area-incompressibility of the spectrin skeleton (being enclosed beneath the lipid bilayer in the erythrocyte membrane) via a nonstiff, and thus efficient, adaptive prestress procedure which accounts for the (locally) isotropic stress imposed by the lipid bilayer on the cytoskeleton. In addition, we investigate the dynamics of healthy human erythrocytes in strong shear flows with capillary number $Ca = O(1)$ and small-to-moderate viscosity ratios $0.001 \leq \lambda \leq 1.5$. These conditions correspond to a wide range of surrounding medium viscosities (4–600 mPa s) and shear flow rates (0.02–440 s^{-1}), and match those used in ektacytometry systems. Our computational results on the cell deformability and tank-treading frequency are compared with ektacytometry findings. The tank-treading period is shown to be inversely proportional to the shear rate and to increase linearly with the ratio of the cytoplasm viscosity to that of the suspending medium. Our modeling also predicts that the cytoskeleton undergoes measurable local area dilatation and compression during the tank-treading of the cells.

INTRODUCTION

Because of the seminal work of Fischer et al. (1), it is known that the erythrocytes elongate and orient to an ellipsoidal-like shape while their membrane tank-treads around the cell when the cells are subjected to a strong shear flow in a more viscous suspending liquid. The frequency of the tank-treading motion F_{tt} was found to increase linearly with the shear rate G of the flow. Recently Fischer (2), via improved experimental measurements, verified the linear increase of the tank-treading frequency F_{tt} with the shear rate, and also found that the slope of this dependence increased weakly with the viscosity of the suspending medium. In addition, Abkarian et al. (3), employing a cell imaging method parallel to the shear plane, found that at low shear stress ($\mu G \approx 0.1$ Pa) erythrocytes present an oscillation of their inclination (which they called swinging motion) superimposed to the long-observed steady tank-treading motion.

We emphasize that studies on the flow dynamics of erythrocytes still constitute a challenging problem in any type of research. Experimental findings are still restricted, owing to the cell's micron size and constraints of the devices (e.g., specific flow-rate regimes or one view-angle (2,3)). In addition, the coupling of the fluid dynamics with the nonlinear membrane tensions prohibits analytical solutions of the erythrocyte motion and limits the usage of the state-of-the-art three-dimensional computational methodologies (e.g., (4,5)). Thus, simplified models have been proposed to describe the tank-treading, swinging, and tumbling motions of erythrocytes in shear flows (e.g., (3,6,7)).

In the area of our interest (i.e., computational investigation), several continuum and molecular-based models have been developed in the recent decades to study erythrocytes. In the continuum models, treating the erythrocyte membrane as a two-dimensional elastic solid with large area-dilatation modulus results in a very stiff problem with high computational cost for three-dimensional investigations (e.g., (4,5)). On the other hand, cytoskeleton-based molecular algorithms were able to model efficiently the global area-incompressibility of the skeleton (e.g., (8–10)) but their applicability to flow problems is usually restricted owing to large computational cost with thus very few three-dimensional flow investigations (e.g., (11)).

This article has thus two main goals:

1. To develop a nonstiff methodology for the efficient determination of erythrocyte dynamics in viscous flows.
2. To investigate the tank-treading motion of the cells in strong shear flows.

By combining the current experience on erythrocyte computational algorithms via both continuum and molecular modelings, we develop a computationally efficient cytoskeleton-based continuum erythrocyte algorithm. In addition, we investigate the dynamics of healthy erythrocytes in strong shear flows and for high surrounding fluid viscosities that match those used in ektacytometry systems (2,12).

Submitted May 27, 2010, and accepted for publication August 24, 2010.

*Correspondence: dimitrak@eng.umd.edu

Editor: Alexander Mogilner.

0006-3495/10/11/2906/11 $2.00

doi: 10.1016/j.bpj.2010.08.048

PROBLEM DESCRIPTION AND COMPUTATIONAL ALGORITHM

Properties of healthy erythrocytes

A human erythrocyte is essentially a capsule (i.e., a membrane-enclosed fluid volume) where the liquid interior (cytoplasm) is a concentrated hemoglobin solution and behaves as a Newtonian fluid with viscosity $\mu_c \approx 6$ mPa s (13,14) at the human body temperature of 37°. In healthy blood and in the absence of flow, the erythrocyte assumes a biconcave discoid shape with a diameter of 7.8 μm, and a thickness varying in 0.8–2.6 μm (15,16). The average human erythrocyte has a surface area of 135 μm^2, and a volume of 94 μm^3 at physiological osmolarity (15). (For purposes of comparison, a sphere of the same volume would have a surface area of only 100 μm^2 and a radius of $a = 2.8$ μm.) Working with experimental observations from interference microscopy, Evans and Fung (15) gave an empirical equation to describe the half-thickness $f(r)$ as a function of the radial distance r from the central axis of symmetry:

$$f(r) = \frac{1}{2}\left[1 - \left(\frac{r}{R_0}\right)^2\right]^{\frac{1}{2}}\left[C_0 + C_2\left(\frac{r}{R_0}\right)^2 + C_4\left(\frac{r}{R_0}\right)^4\right]. \tag{1}$$

At physiological osmolarity (300 mO), $R_0 = 3.91$ μm, C_0 – 0.81 μm, C_2 – 7.83 μm, and $C_4 = -4.39$ μm. In our computations, this shape is employed as the elastic reference shape (i.e., the shape of the erythrocyte under quiescent conditions), in agreement with experimental findings which have demonstrated the erythrocyte shape memory, i.e., the fact that after tank-treading an erythrocyte will always reform its two dimples in the same distinct loci on the membrane (17).

Fluid dynamics

We consider an erythrocyte in an infinite ambient fluid undergoing flow. The interior and exterior fluids are Newtonian, with viscosities $\mu_c = \lambda\mu$ and μ, respectively. Owing to the external flow and the cell's small size, the gravitational effects of a density difference between the two fluids (if any) are negligible. In low-Reynolds-number flows, the governing equations in both fluids are the Stokes equations and continuity.

The velocity $\boldsymbol{u}$ at each point $\boldsymbol{x}$ on the erythrocyte's surface S_B may be determined by the boundary integral equation

$$(1 + \lambda)\boldsymbol{u} - 2\boldsymbol{u}^\infty = -\frac{1}{4\pi\mu}\int_{S_B}[\boldsymbol{S}\cdot\Delta\boldsymbol{f} - (1-\lambda)\mu\boldsymbol{T}\cdot\boldsymbol{u}\cdot\boldsymbol{n}]dS, \tag{2}$$

where the tensors $\boldsymbol{S}$ and $\boldsymbol{T}$ are known functions of geometry while the unit normal $\boldsymbol{n}$ points into the surrounding fluid (18). Note that $\Delta\boldsymbol{f}$ is the surface stress and $\boldsymbol{u}^\infty$ the imposed external flow, e.g., a simple shear flow $\boldsymbol{u}^\infty = G(z, 0, 0)$, where G is the shear rate.

Our membrane description is based on the well-established continuum approach and the theory of thin shells (19). We emphasize that the thin-shell theory has proven to be an excellent description of the membrane for a wide range of artificial capsules and for red blood cells, where the membrane thickness is several orders-of-magnitude smaller than the size of the capsule/cell (19,20). To describe the tensions on the erythrocyte membrane, we use the strain-hardening constitutive law of Skalak et al. (21), which accounts for both shearing and area-dilatation resistance.

The surface stress on the membrane is determined by the in-plane stresses, i.e., $\Delta\boldsymbol{f} = -\nabla s\cdot\boldsymbol{\tau}$, where the in-plane stress tensor $\boldsymbol{\tau}$ is described by the law of Skalak et al., which relates $\boldsymbol{\tau}$'s eigenvalues (or principal elastic tensions τ_β^P, $\beta = 1, 2$) with the principal stretch ratios λ_β by

$$\tau_1^P = \frac{G_s\lambda_1}{\lambda_2}\left(\lambda_1^2 - 1 + C\lambda_2^2\left[(\lambda_1\lambda_2)^2 - 1\right]\right) \tag{3}$$

(to calculate $\tau^P{}_2$, reverse the λ_β subscripts (19)). The shearing modulus G_s introduces the (elastic) capillary number $Ca = \mu Ga/G_s$ as the ratio of viscous forces to shearing forces on the membrane. Here μ is the viscosity of the surrounding fluid and a is the radius of a sphere with the same volume as the erythrocyte (i.e., $a = 2.8$ μm at physiological osmolarity).

Note that the dimensionless parameter C is associated with the area-dilatation modulus (scaled with the shearing modulus). Analysis in the limit of small deformations shows that the area-dilatation modulus is

$$K = G_s(1 + 2C),$$

while the surface Young modulus is (19)

$$E_s = 2G_s(1 + 2C)/(1 + C).$$

The capsule's time evolution is determined via the kinematic condition at the interface $d\boldsymbol{x}/dt = \boldsymbol{u}$. The numerical solution of the interfacial problem is achieved through our interfacial spectral boundary element method for membranes (18,20). The initial biconcave discoid interface is divided into a moderate number N_E of elements (e.g., see Fig. 2); on each element all geometric and physical variables are discretized by using $(N_B - 1)$-order Lagrangian interpolation based on the zeros of orthogonal polynomials. The accuracy of our results was verified by employing smaller time steps and different grid densities for several representative cases. (In particular, we employed $N_E = 10$ spectral elements with $N_B = 11$–14 basis points; for the time integration, we employed the fourth-order Runge-Kutta scheme with time step in the range $\Delta t = 10^{-5}$–10^{-4}.) More details on our interfacial spectral boundary methods may be found in our earlier publications (18,20).

Description of erythrocyte membrane

The erythrocyte membrane is a complex multilayered object consisting of a 4-nm-thick lipid bilayer and an underlying elastic network of spectrin which is anchored to the lipid bilayer through proteins. The lipid bilayer is essentially a two-dimensional incompressible fluid with no shear resistance, but the spectrin skeleton anchored to it exhibits shear resistance like a two-dimensional elastic solid (16). At low strains, optical tweezers have found that the membrane-shear modulus is $G_s = 2.5 \pm 0.4$ μN/m (22). The area-dilatation modulus of the membrane (resulting from the lipid bilayer) is $K = O(1$ N/m) and thus $C = O(10^5) \gg 1$ (13).

Continuum computational models commonly treat the erythrocyte membrane as a two-dimensional elastic solid with large area-dilatation modulus, e.g., by employing the Skalak et al. law (Eq. 3) with large C. This introduces computational difficulties especially for three-dimensional problems (e.g., see (4,5)). In the case of the erythrocyte, the area-dilatation resistance is much higher than its shearing resistance (the parameter $C = O(10^5)$), which results in a very stiff problem. That is, the dilatation tensions develop over a short timescale, which requires a very small time step due to the employed explicit time integration, but shearing tensions develop over a long timescale, which necessitates a long simulation runtime. Previous investigators who used this approach weakened this requirement by employing a much smaller moduli ratio than the true physical value (e.g., $C = O(100)$ (4,5)), in order to make the problem computationally feasible. However, even this smaller C, needed to achieve nearly area-incompressibility, results in a large computational cost for three-dimensional computations owing to the associated small time steps.

Another consideration for the description of the erythrocyte membrane is its measurable bending resistance with reduced bending modulus (with respect to its shearing resistance) (23),

$$K_B/a^2G_s \;=\; O\left(10^{-3}\right).$$

This is not large enough to affect the overall cellular deformation (14), but it may prevent local buckling which could otherwise occur under certain flow conditions. A realistic model for the erythrocyte membrane must have a way to account for this, although it will not necessarily do so by representing explicitly the formation of bending moments.

Finally, a computational model may account for the membrane viscosity, which is $O(10^{-7})$ Ns/m (24). In the continuum description this is usually achieved by the linear addition of a surface viscosity model (e.g., the Kelvin-Voigt model) to the equation describing the membrane stresses (e.g., see Eq. 3 above (25)). However, such consideration raises additional questions on the surface viscosity model appropriate for the erythrocyte membrane and more generally on the linear (versus nonlinear) addition of a surface viscosity model into the membrane stresses. Because the main goal of this article is to remove the stiffness in the erythrocyte modeling associated with the local area-incompressibility of the lipid bilayer, we do not explicitly consider the viscosity of the erythrocyte membrane in our computational model (which is the same approach used by earlier continuum models (4,5,7)).

NONSTIFF CYTOSKELETON-BASED CONTINUUM MODELING

As discussed in Description of Erythrocyte Membrane, the existing continuum membrane description focuses on the lipid bilayer where it enforces local area-incompressibility, e.g., via $C \gg 1$. The shearing tensions of the spectrin cytoskeleton are then transferred to the lipid bilayer and accounted for via the first term (containing G_s) in the law of Skalak et al. The requirement to enforce local area-incompressibility of the lipid bilayer results in a stiff computational problem as explained previously. However, this formulation does not describe the spectrin cytoskeleton (beyond the transferred shearing tensions) because the cytoskeleton can undergo local area changes under the constraint of fixed total area being enclosed beneath the lipid bilayer (26).

To derive a computationally efficient model for the erythrocyte membrane, in this work we focus on the spectrin cytoskeleton. This interface has shearing resistance; it preserves its total area but may allow local area changes, while (local) area-incompressibility tensions are transferred to it from the lipid bilayer. Thus, we assume that our spatial discretization explicitly represents the spectrin network, and not the lipid bilayer. To describe the dynamics of the cytoskeleton we employ a continuum modeling; in particular, the cytoskeleton is modeled as a two-dimensional elastic solid with shearing and area-dilatation resistance that follows the material law of Skalak et al. The numerical solution of the interfacial problem is achieved through our interfacial spectral boundary element method for membranes as described earlier in Fluid Dynamics.

The mechanism by which a lipid bilayer enforces area-incompressibility is a (locally) isotropic surface stress as happens for fluid vesicles (27). An isotropic surface stress can also be generated with an elastic membrane model by employing prestress. (For example, Lac and Barthès-Biesel (28) employed small prestress to represent elevated internal capsule pressure and prevent local buckling.) Applying a prestress into an elastic membrane model applies an isotropic surface tension to an undeformed shape, or adds a near-isotropic tension to a deformed shape. The prestress can be generated by shrinking or expanding the elastic reference shape, without changing the current shape, or by scaling the stretch ratios λ_β.

Based on our formulation, the in-plane tension $\boldsymbol{\tau}$ can be written as

$$\boldsymbol{\tau} = \boldsymbol{\tau}^E + \boldsymbol{\tau}^I,$$

where $\boldsymbol{\tau}^E$ is the tension produced by elastic deformation of the spectrin network, and $\boldsymbol{\tau}^I$ is an isotropic tension such that local surface-area incompressibility ($\nabla_S \cdot \boldsymbol{u} = 0$) would hold for the lipid bilayer, which we do not represent explicitly. Using only the elastic law and applying a prestress, the new tension produced can be written as

$$\boldsymbol{\tau} = \boldsymbol{\tau}^E + \boldsymbol{\tau}^P,$$

where $\boldsymbol{\tau}^E$ is the tension produced with no prestress, and $\boldsymbol{\tau}^P$ is the portion of the tension tensor added by the application of prestress. When the surface is undeformed, $\boldsymbol{\tau}^P$ is perfectly (locally) isotropic. When the surface is deformed, $\boldsymbol{\tau}^P$ is still near-isotropic, with the degree of deviation from being perfectly isotropic determined by the magnitude of the parameter C for the constitutive law of Skalak et al. (small C values introduce a larger nonisotropic component and thus very small C should be avoided). Thus, we want to approximate effect of the surface tension $\boldsymbol{\tau}^I$ of the lipid bilayer by using a prestress to apply the tensor $\boldsymbol{\tau}^P$ such that area is globally conserved.

Following Lac and Barthès-Biesel (28), we define the prestress parameter α such that all lengths in the undeformed capsule would be scaled by $(1 + \alpha)$, relative to the reference shape. Thus, for $\alpha = 0.05$, for instance, the undeformed capsule would be 5% larger than the reference. Note that this is mathematically equivalent to scaling the stretch ratios by $(1 + \alpha)$. Fig. 1 *a* shows the normalized change in area over a short time for $\alpha = 0.05$ and 0.1. It is apparent that prestress counteracts the shearing forces in the flow, to dampen the initial surface area rise. However, area oscillations of >4% are still observed for the larger prestress. Further, as the simulation continues, the prestress causes contraction, and the surface area decreases significantly below its initial value.

During transient dynamics of erythrocyte deformation (such as its tank-treading motion in shear flows), the cytoskeleton prestress adjusts itself while the surface area of the skeleton is (globally) fixed. While one may augment the interfacial system by adding a constraint of fixed global skeleton area and solving for the prestress, the nonlinear nature of this constraint significantly complicates a continuum algorithm. To determine the cytoskeleton prestress efficiently, in this study we utilize an adaptive prestress procedure, based on a standard discrete velocity-type proportional-integral-derivative (PID) controller (29). The goal is to solve for the prestress continually throughout the transient dynamics via the control equation

$$\alpha_n = \alpha_{n-1} + \big(K_p + K_i + K_d\big)e_n - \big(K_p + 2K_d\big)e_{n-1} + K_d e_{n-2} \tag{4}$$

to achieve a constant skeleton surface area. The prestress α_n is adjusted at each time step based on α_{n-1} from the previous step, the current error e_n in surface area, and, for iterations after the initial two, the error from the previous two steps e_{n-1} and e_{n-2}. K_p, K_i, and K_d are the proportional, integral, and derivative control parameters, respectively. Using mainly the parameter settings $K_p = K_i = K_d = 1$, we obtained excellent control performance; Fig. 1 *a* shows that the adaptive prestress method maintains a near-constant surface area. We also obtained identical results using smaller values for the control parameters, e.g.,

$$\{K_p, K_i, K_d\} = \{1, 0.2, 0\}, \{0.1, 0.1, 0.1\}, \text{ and } \{0.1, 0.1, 0\}.$$

Thus, no attempt was made to tune further the control parameters.

Via the adaptive prestress method, our interfacial algorithm produces stable solutions for the erythrocyte dynamics over long time periods in several flow types tested (e.g., shear and planar extensional flows). In all cases, the ratio

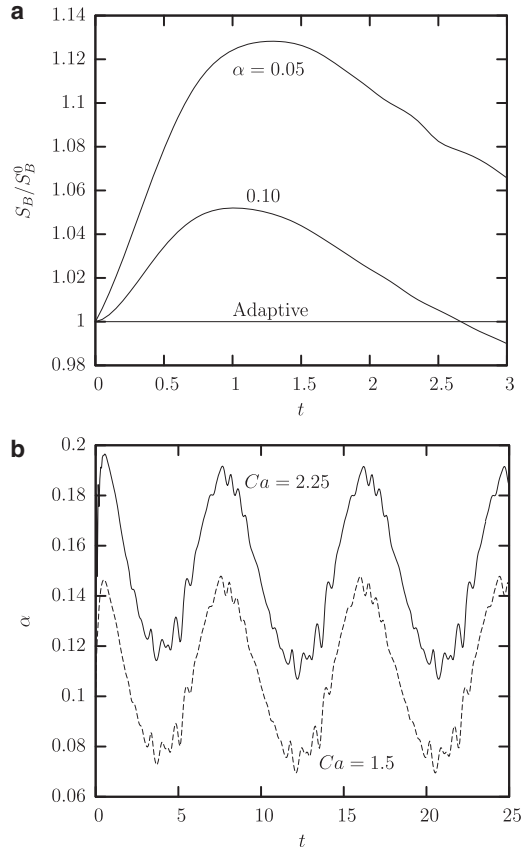

FIGURE 1 (*a*) Time evolution of the surface area S_B of our (computational) erythrocyte (scaled by the surface area S^0_B of its biconcave-disk reference shape) in a simple shear flow with two different levels of prestress, $\alpha = 0.05$ and 0.1. Also shown are the results with adaptive prestress, which effectively maintains a constant surface area. Parameters: $Ca = 1.5$ and $\lambda = 0.1$. Law of Skalak et al. (21) with $C = 1$. (*b*) Time evolution of the prestress parameter α for a simple shear flow with $Ca = 1.5$ and 2.25 and $\lambda = 0.1$, using the law of Skalak et al. with $C = 1$, with our adaptive prestress method.

of the surface area of the deformed shape to that of the resting shape is always

$$|1 - S_B/S_B^0| \leq 10^{-4}.$$

We emphasize that our adaptive PID prestress procedure is an efficient procedure to determine the cytoskeleton prestress and mathematically equivalent to the full solution of the augmented nonlinear constrained interfacial system.

It is of interest to note that in shear flows the prestress parameter α shows periodic oscillations over time with a period half that for the tank-treading motion, as shown in Fig. 1 *b*, owing to the erythrocyte's swinging motion (3,7). For a given viscosity ratio λ and Skalak parameter C, by increasing the capillary number Ca, the prestress parameter increases owing to the higher hydrodynamic forces which require stronger membrane tensions. As seen in Fig. 1 *b*, for $Ca = 1.5$ the adaptive prestress α is < 0.15 throughout the simulation, and for $Ca = 2.25$, $\alpha \leq 0.2$ throughout the simulation. We emphasize that the small noise seen in the time evolution of the prestress parameter (probably due to the fact that the control is very aggressive in keeping a negligible variation of the surface area S_B) does not affect the time evolution of the interfacial shape, e.g., the evolution of the erythrocyte dimensions or its inclination angle.

Utilizing different parameters C for the law of Skalak et al., our method shows that C near 1 or higher produces identical results for the erythrocyte dynamics. (As discussed previously, very small C should be avoided, i.e., $C \leq 0.5$, because they introduce a larger nonisotropic component in the prestress tension and underestimate the erythrocyte deformation.) In our modeling, the exact value of $C \geq O(1)$ is not important because both the term in the equation for the law of Skalak et al. (Eq. 3) where the parameter C appears and the prestress produce isotropic tensions; thus, the parameter C and prestress complement each other in producing the necessary isotropic tensions to globally preserve the area of the spectrin skeleton.

Therefore in our work we have employed the dimensionless parameter $C = 1$, which produces a nonstiff problem and does not increase the computation cost. An additional advantage is that prestress helps prevent local buckling, thus fulfilling the role of bending resistance for a system like the erythrocyte where the reduced bending modulus is very low. It is of interest to note that $C = 1$ also represents well the spectrin skeleton because at low strains optical tweezers have found the area-dilatation and shear moduli of the skeleton to be $K^{sp} = 4.8 \pm 2.7$ μN/m and $G_s^{sp} = 2.4 \pm 0.7$ μN/m (30), which suggests that, for the spectrin skeleton, $C^{sp} = 0.5$.

ERYTHROCYTE DYNAMICS IN STRONG SHEAR FLOWS

In this section we investigate computationally the erythrocyte dynamics in a simple shear flow $\boldsymbol{u}^\infty = G(z, 0, 0)$ for high capillary numbers $Ca = O(1)$ and small-to-moderate viscosity ratios $0.001 \leq \lambda \leq 1.5$.These conditions correspond to a wide range of medium viscosities (4–600 mPa s) and shear flow rates (0.02–440 s^{-1}). The Reynolds number for both the surrounding and the cytoplasm flows is always negligible owing to the cell's small size. Our flow conditions match those used in ektacytometry systems (1,2,12).

At the flow initiation, the erythrocyte has its equilibrium biconcave discoid shape at physiological osmolarity given by Eq. 1. In addition, the initial position of the undeformed geometry is at an orientation angle $\Phi = 20^\circ$ with the flow direction, i.e., the x axis. All reported times are scaled with the flow timescale G^{-1}.

It is of interest to note that our computations depend only on two dimensionless parameters—i.e., the capillary numbers Ca and the viscosity ratio λ. When we convert our results to actual variables (see later in Figs. 4 and 5 *a*), we use $\mu_c = 6$ mPa s and $a = 2.8$ μm, as well as the average value of the membrane shear modulus at low strains $G_s = 2.5$ μN/m (22) because our computations involve rather small and moderate deformations. (In our work, the cell dimensions vary in the range of −20–40%.) Employing smaller or higher values of G_s does not change our results presented in these two figures but shifts our computed points to smaller or higher shear rates, respectively.

After an initial transient period, the erythrocyte assumes an inclined ellipsoidal conformation owing to the strong shear flow while its membrane tank-treads around the cell owing to the rotational component of the shear flow, as found in experimental systems (e.g., (1,2)). For $Ca = 1.5$ and $\lambda = 0.1$, the transition from a biconcave disk to an ellipsoidal shape occurs from $t = 0$ to $t = 2$, as illustrated in Fig. 2. In addition, the biconcave reference shape introduces periodic oscillations into the tensions produced as the deformed erythrocyte tank-treads, i.e., the dimple regions of the original biconcave geometry deform differently than the edge regions as they pass around the surface contour (3,7). Thus, at steady state, the cell shape oscillates around a mean value with a period half that for the tank-treading motion (owing to the symmetry of the biconcave reference shape), as experimentally found recently for erythrocytes in weak shear flows (3).

Comparison to ektacytometry results

Ektacytometry systems have been developed to measure the deformability of the erythrocyte by observing the deformation behavior of individual cells, or average deformabilities for populations of cells (1,2,12). In these devices, the flow pattern is a simple shear flow (or a good approximation of it) while the deformed erythrocyte is not observed in the plane of shear but from above the shear plate device. In our computations, $\boldsymbol{u}^\infty = G(z, 0, 0)$ and thus the plane of shear is the xz plane. In our terminology, we can say that

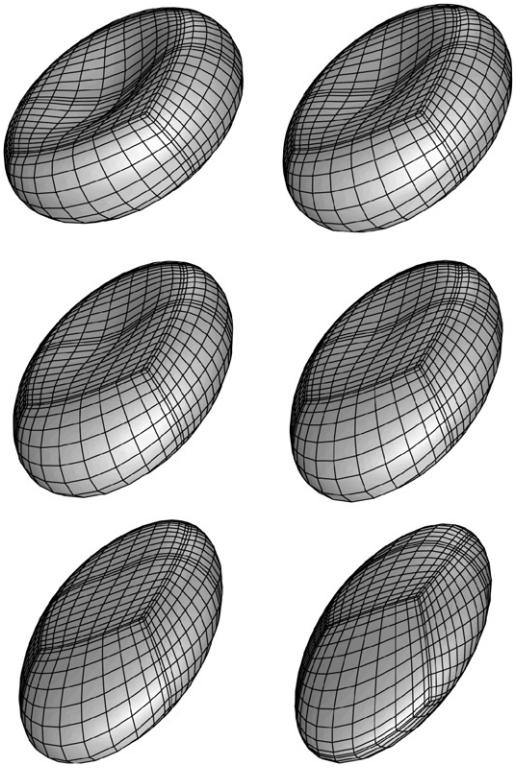

FIGURE 2 Shape transition from a biconcave disk to an ellipsoid for an erythrocyte in a simple shear flow with $Ca = 1.5$ and $\lambda = 0.1$. The erythrocyte shape is plotted row-wise at times $t = 0$, 0.2, 0.4, 0.6, 1, and 2, as seen slightly askew from the shear (i.e., xz) plane.

ektacytometry observes the deformed erythrocyte projected as an ellipse on the xy plane.

The deformation parameter computed from the largest and smallest semiaxes of this ellipse, L_x and L_y, respectively, and reported by researchers using ektacytometry, we will denote D_{xy}. Note that

$$D_{xy} = (L_x - L_y)/(L_x + L_y).$$

Because ektacytometry does not follow individual cells over time but uses a large number of them, and because the erythrocytes' shape oscillates with time in a shear flow, the experimentally reported deformation D_{xy} corresponds to the average value of the cells deformation in the xy plane over time and over the erythrocyte population.

Fig. 3 shows results from ektacytometry (12) compared with our computational data for the time-averaged deformation D_{xy} at steady-state for a range of high capillary numbers. Note that the viscosity ratio for ektacytometry systems usually ranges between 0.1 and 0.2; thus, in Fig. 3 we include our results for both viscosity ratios. We emphasize that the membrane viscosity does not affect the erythrocyte orientation (11) and deformation in shear flows (Dr. D. A. Fedosov and Prof. G. E. Karniadakis, Brown University, personal communication, 2010); thus, our results on the ektacytometry deformation are not affected by the omission of membrane viscosity in our computations.

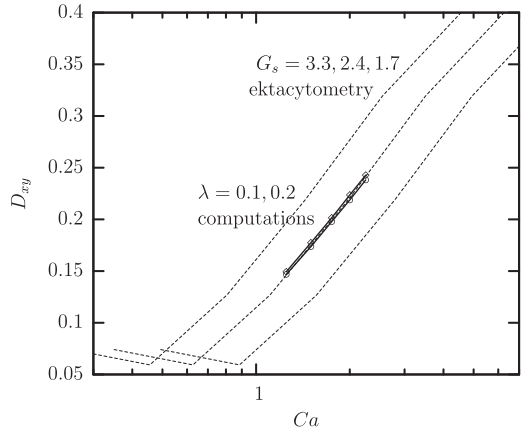

FIGURE 3 Comparison of our computational results with ektacytometry findings reported in Fig. 3 of Hardemann et al. (12). The experimental results for the ektacytometry deformation D_{xy} (*dashed lines*) were converted to the capillary number domain using $G_s = 3.3$, 2.4, and 1.7 μN/m. (Note that these experimental measurements via the LORCA ektacytometer have negligible standard deviation (12).) Also displayed (as *solid lines* with data points) is the time-average deformation D_{xy} computed by our method at steady state for $\lambda = 0.1$ and 0.2.

Our computations capture two important aspects of the relationship between D_{xy} and capillary number (or wall shear stress). First, the relationship is logarithmic for this range of capillary numbers. Second, using a log-scale for capillary number, our computations produce a slope consistent with the experimental results. In addition, our results provide insight on the shear modulus of the erythrocyte membrane at low strains. In Fig. 3 we have converted the experimental results for the ektacytometry deformation D_{xy} from the wall shear stress $\sigma_{wall} = \mu G$ to the capillary number domain $Ca = a\sigma_{wall}/G_s$ by using $G_s = 1.7$, 3.3 μN/m, i.e., two standard deviations around the mean value found by optical tweezers, $G_s = 2.5$, 0.4 μN/m (22). As seen in this figure, our computations fall inside the range valid for most red blood cells. When we convert the experimental data using $G_s = 2.4$ μN/m, the experimental and computational curves coincide as shown in Fig. 3, which may suggest that the sample used in the experimental measurement had a shear modulus very close to the average value found by optical tweezers, $G_s = 2.5$ μN/m (22).

Our computational results on the shear rate dependence of the tank-treading frequency F_{tt} (defined as the inverse of the tank-treading period P_{tt}) of red cells in a simple shear flow are shown in Fig. 4. Our computations show that the tank-treading frequency F_{tt} increases linearly with the shear rate, as reported in the experimental findings of Fischer et al. (1) and other recent experiments (2).

We emphasize that our computations do not account for the viscosity of the erythrocyte membrane which is expected to slow down the tank-treading motion. If we assume that the membrane viscosity is the main reason for the fact that

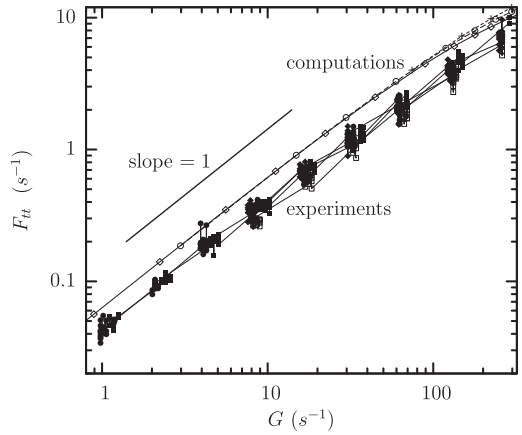

FIGURE 4 Comparison of our computational results with experimental findings from Donor 3 reported in Fig. 2 of Fischer (2) for the tank-treading frequency F_{tt} as a function of the shear rate G in a log-log plot. The computational results are valid for capillary number $Ca = 1.5$, 2, and 2.25 (symbols $\diamond$, $\bigcirc$, and $+$, respectively) and viscosity ratio λ in the range [0.001, 1]. The experimental results are valid for surrounding medium viscosity $\mu = 12.9$, 28.9, 53.9, and 109.3 mPa s (symbols $\square$, $\blacklozenge$, $\bullet$, and $\blacksquare$, respectively) measured at room temperature. Also displayed is a solid line with slope 1 to show the linear increase of F_{tt} with the shear rate.

our computations predict a higher tank-treading frequency as shown in Fig. 4, then our comparison suggests that the membrane viscosity slows down the tank-treading motion by a factor close to 2. This is consistent with the estimation of Fischer (24) that in the tank-treading erythrocytes the energy dissipation in the membrane is of the same order of magnitude as in the cytoplasm.

Dependence of the tank-treading frequency on the medium viscosity

We investigate now the dependence of the tank-treading frequency on the medium viscosity. As seen in Fig. 5 *a*, we found that the slope of this dependence decreases weakly with the viscosity ratio $\lambda = \mu_c/\mu$ and thus it increases weakly with the viscosity of the suspending medium μ, as reported in the recent experimental study of Fischer (2).

Proceeding further, we were able to identify the exact dependence of the tank-treading speed on the viscosity of the suspending medium. As seen in Fig. 5 *b*, the tank-treading period $P_{tt} = {F_{tt}}^{-1}$ (i.e., the time required for a full revolution of the erythrocyte membrane) increases linearly with the viscosity ratio λ while it is inversely proportional to the shear rate G. Thus,

$$F_{tt} = \frac{G}{C_1\lambda + C_0} = \frac{G}{C_1\mu_c/\mu + C_0}, \qquad (5)$$

where the constants are $C_1 \approx 10.5$ and $C_0 \approx 16$.

The increase of the tank-treading period with the viscosity ratio is consistent with the increased hydrodynamic forces in the cytoplasm, which slow down the rotation of the inner fluid and thus, the erythrocyte membrane.

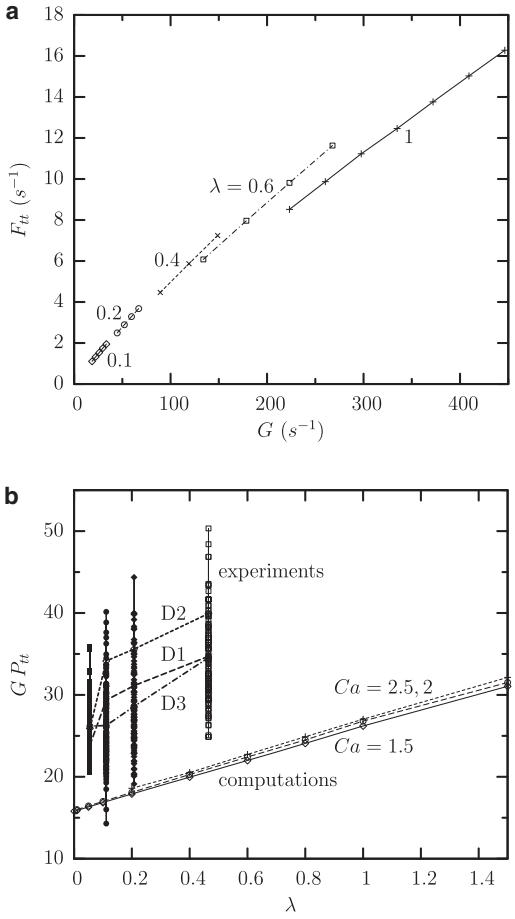

FIGURE 5 (*a*) Tank-treading frequency F_{tt} as a function of the shear rate G for viscosity ratio $\lambda = 0.1$, 0.2, 0.4, 0.6, and 1 and capillary number Ca in the range [1.25, 3]. (*b*) Tank-treading period GP_{tt} as a function of the viscosity ratio λ for $Ca = 1.5$, 2, and 2.25 (symbols $\diamond$, $\bigcirc$, and $+$, respectively). The regression lines for the three flow rates are $GP_{tt} = 10.2\lambda + 15.8$, $GP_{tt} = 10.5\lambda + 16.0$, and $GP_{tt} = 10.5\lambda + 16.4$. Also included are the experimental findings from Fig. 2 of Fischer (2); these data are valid for surrounding medium viscosity $\mu = 12.9$, 28.9, 53.9, and 109.3 mPa s (symbols $\square$, $\blacklozenge$, $\bullet$, and $\blacksquare$, respectively) and were converted to viscosity ratio λ using $\mu_c = 6$ mPa s. The lines denoted as $D1$, $D2$, and $D3$ connect the arithmetic average for a given viscosity ratio of the experimental data from Donors 1, 2, and 3, respectively.

We note that our results are in very good agreement with the computations of Sui et al. (5), who employed the traditional continuum erythrocyte modeling utilizing the law of Skalak et al. with large C and who also neglected the membrane viscosity. Their study is restricted to unity/viscosity ratio, and found a nondimensional frequency $2\pi/(GP_{tt}) = 0.23$ for capillary number $Ca = 1.5$ as shown in their Fig. 7. Our computations for this viscosity ratio and capillary number shown in Fig. 5 *b* reveal that this frequency is 0.24.

To provide a better comparison between our own predictions and the experimental findings, in Fig. 5 *b* we also include the data from Fig. 2 of Fischer (2), which are valid for four surrounding medium viscosities, $\mu = 12.9$, 28.9,

53.9, and 109.3 mPa s. For a given viscosity, the experimental findings show a wide variation, probably due to the inherent differences between erythrocytes. Owing to the variation of the experimental data and the fact that they are valid for only four viscosity ratios, it is difficult to verify or reject our computation prediction on the relationship between GP_{tt} and λ. However, connecting the arithmetic average for a given viscosity ratio of the data from the three donors (lines $D1$, $D2$, and $D3$ in Fig. 5 *b*) does suggest a linear increase of GP_{tt} with λ for the three largest viscosity ratios. Our understanding is that experimental findings for more of the surrounding medium viscosities are needed, accompanied, if possible, with measurements of the actual properties of the cells to reduce the data variation.

Is the surface area of the spectrin skeleton locally preserved?

Owing to the fact that the surface area of the spectrin skeleton is globally, but not locally, preserved, a question naturally arises on the magnitude of the local area changes of the cytoskeleton for the problem studied in this work (i.e., tank-treading of erythrocytes in strong shear flows).

This problem has been studied by Fischer (26) who, via a simplified continuum model, concluded that in fast erythrocyte processes (such as tank-treading in vivo or in ektacytometry systems) there is no time for local area changes while quasistatic (i.e., long) processes (such as micropipette experiments (31)) may be accompanied with local area variations of the spectrin skeleton. (Discussion on older modeling of cytoskeleton's local surface area can also be found in Fischer's work (26).)

Before we present the results of our cytoskeleton-based modeling, we wish to clarify the following issues involving the earlier work/modeling and its connection to our own modeling.

First, Fischer's predictions are rather rough for a number of reasons, including the simplifications of the employed model and the estimate of the value of the parameters involved in his model, as the author commented in the conclusions of his article (26). Thus, the true skeleton behavior can diverge significantly from Fischer's predictions.

Second, our understanding is that Fischer's analysis formally applies to the local area changes during the two processes he studied, and not with respect to the equilibrium biconcave disk geometry. For example, his conclusion for local area incompressibility during tank-treading in vivo or in ektacytometry systems refers to local area changes during the steady-state tank-treading motion. However, the tank-treading ellipsoidal erythrocyte in strong shear flows differs significantly from its equilibrium biconcave disk shape; thus, Fischer's conclusion may permit local area changes between the equilibrium biconcave and tank-treading ellipsoidal shapes.

In addition, we emphasize that conceptually Fischer's continuum modeling (26) differs significantly from our own. Fischer described the integral proteins which connect the cytoskeleton with the lipid bilayer as fenceposts on the cytoskeleton, and assumed that the controlling step is the relative motion of these proteins and the lipids. As described in the earlier work, a local change in surface area of the cytoskeleton involves a relative motion between lipid molecules and intrinsic proteins; this motion requires sufficient time owing to friction. For fast processes (e.g., tank-treading in ektacytometry systems or in vivo), Fischer concluded that there is no time for a relative motion, and thus, the surface area of cytoskeleton should be locally conserved. On the other hand, in our continuum membrane modeling we do not consider explicitly the intrinsic proteins; therefore, we assume that the controlling step in the deformation of the cytoskeleton's surface area is the interaction of the hydrodynamic forces of the applied shear flow with the membrane tensions. That is, we assume that the intrinsic proteins diffuse fast enough to accommodate any local area changes imposed on the cytoskeleton by the applied flow.

In Fig. 6 *a*, we present the time evolution of the differential surface area for four representative spectral discretization points on the erythrocyte membrane for typical shear flow conditions (i.e., $\lambda = 0.1$ and $Ca = 1.5$). Our computational results for all the discretization points used show that, with respect to the equilibrium biconcave disk geometry, the cytoskeleton local area increases by almost 30% and decreases by almost 20%. In addition, during the steady-state tank-treading motion, the cytoskeleton local area changes by nearly $\pm 10\%$.

Thus, for the physical problem studied in this work, the cytoskeleton undergoes measurable local area dilatation and compression. To show how much these local area changes accumulate in larger portions of the cytoskeleton, in Fig. 6 *b*, we plot the time evolution of the surface area of the spectral elements used in our computations. With respect to the equilibrium shape, large portions of the cytoskeleton show an almost 17% increase in surface area; however, during the steady-state tank-treading motion, the same surface elements show a smaller area change of almost $\pm 8\%$. We note the similar results that we obtain for higher viscosity ratios, e.g., $\lambda = 1$.

Our computational modeling also predicts that the dimple regions of the quiescent biconcave-disk shape (e.g., the two spectral elements forming the dimple in the first erythrocyte view seen in Fig. 2) show the largest area increase; that the edge regions along the flow direction show the largest area decrease; and that the lateral edge regions show the smallest area variation.

It of interest to note that both the differential surface area S_P and the surface area of the spectral elements S_E presented in Fig. 6 show periodic oscillations around a mean value owing to the cell's swinging motion; the period of oscillations is half that for tank-treading motion, as found for the

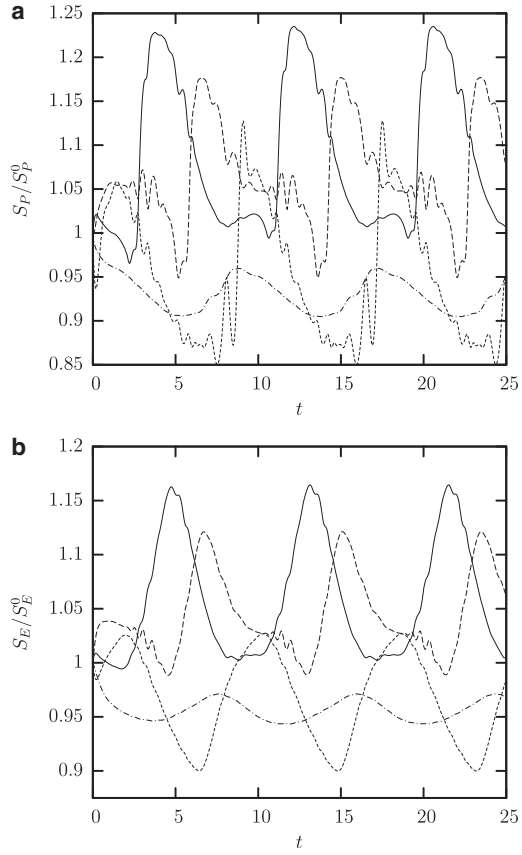

FIGURE 6 (*a*) Time evolution of the differential surface area S_P (scaled with its original value $S_P{}^0$) for the spectral discretization point at the middle of the spectral elements for an erythrocyte tank-treading in shear flow with $\lambda = 0.1$ and $Ca = 1.5$. Note that S_P is determined based on the standard mathematical definition of the differential area of a surface $\mathrm{x}(\xi,\eta)$, $S_P = \|\frac{\partial \mathrm{x}}{\partial \xi} \times \frac{\partial \mathrm{x}}{\partial \eta}\| \mathrm{d}\xi\, d\eta$. (*b*) Time evolution of the surface area of the spectral elements S_E (scaled with its original value $S_E{}^0$) for the same conditions as in panel *a*. Note that out of the $N_E = 10$ spectral elements used in our computations, only four are independent (and show different behavior) owing to symmetry reasons. With respect to the first cell shown in Fig. 2, the location of the spectral elements presented here is (*solid line*) upper dimple; (*long-dashed line*) lower dimple; (*short-dashed line*) edge region along the flow direction; and (*dash-dotted line*) lateral edge. (The phase difference in the time evolution of the two dimple elements results from their different location; e.g., the middle point on the lower dimple needs more time to go to the edge of the erythrocyte's ellipsoidal shape during tank-treading.)

inclination oscillations for erythrocytes in weak shear flows (3,7). We also note that the small noise in the curves shown in Fig. 6 is of numerical origin (due to the local nature of the properties plotted and the finite discretization) and irrelevant to the present adaptive prestress procedure, because we also find the same noise for these properties even in our computations with capsules in shear flows.

DISCUSSION

In this article, we have developed a computationally efficient cytoskeleton-based continuum erythrocyte algorithm. The cytoskeleton is modeled as a two-dimensional elastic solid with comparable shearing and area-dilatation resistance that follows the material law of Skalak et al. (21). It is of interest to note that in their 1973 article (21), Skalak et al. proposed to use a large area-dilatation resistance for the erythrocyte modeling (or $C \gg 1$) because they modeled the entire membrane, i.e., the idea that the cytoskeleton can undergo local area changes came up later (26). However, the law of Skalak et al. is general and able to describe any (strain-hardening) membrane with any area-dilatation resistance (e.g., (18,19)). Our modeling enforces the global area-incompressibility of the spectrin skeleton via a nonstiff, and thus efficient, adaptive prestress procedure which accounts for the (locally) isotropic stress imposed by the lipid bilayer on the cytoskeleton. The prestress procedure also helps prevent local buckling and thus accounts for the role of the bending resistance of the erythrocyte membrane. In this article we have combined our nonstiff continuum erythrocyte modeling with our spectral boundary element method for elastic capsules (18) to solve the interfacial problem; however our cytoskeleton modeling is general and can be combined with any membrane interfacial method.

As discussed in Nonstiff Cytoskeleton-Based Continuum Modeling, our understanding is that the spectrin skeleton should be under prestress owing to the area-incompressibility tensions transferred to it from the lipid bilayer. It is of interest to note that the cytoskeleton-based molecular model of Discher et al. (9) also found that prestress is necessary for optimal agreement with fluorescence imaging experiments in the case of the large static deformations in micropipette aspiration. More generally, cellular tensegrity models which include cytoskeleton prestress have also been proposed for mammalian cells to link mechanics to structure at the molecular level (32).

During transient dynamics of erythrocyte deformation (such as its tank-treading motion in shear flows), the cytoskeleton prestress should adjust itself while the surface area of the skeleton is (globally) fixed. While one may augment the interfacial system by adding a constraint of fixed global skeleton area and solving for the prestress, the nonlinear nature of this constraint significantly complicates a continuum algorithm. In order to determine the cytoskeleton prestress efficiently, in this study we utilize a PID controller so that the surface area of the skeleton is (globally) fixed. The time evolution of prestress shown in Fig. 1 *b* does not suggest an unrealistic prestress adjustment to satisfy the fixed surface area, while the PID prediction of the cytoskeleton prestress is mathematically equivalent to the full solution of the augmented nonlinear constrained interfacial system.

In addition, we have investigated the dynamics of healthy human erythrocytes in strong-shear Stokes flows with capillary number $Ca = O(1)$ and small-to-moderate viscosity ratios $0.001 \leq \lambda \leq 1.5$ that match the conditions used in

ektacytometry systems. Our computations capture two important aspects of the relationship between cell deformation and capillary number (or wall shear stress): the dependence is logarithmic for the employed range of shear rates, while using a log-scale for capillary number our method produces a slope consistent with experimental results. By comparing our computational results and ektacytometry findings (12) on the cell deformation, our computations fall inside the range for G_s valid for most red blood cells at low strains, i.e., 1.7–3.3 μN/m (22).

Our computations show that the tank-treading frequency F_{tt} of the erythrocyte membrane increases linearly with the shear rate, as reported in the experimental findings of Fischer et al. (1) and other recent experiments (2). In addition, our results suggest that the membrane viscosity (which is not accounted for in our present computations) slows down the tank-treading motion by a factor close to 2. Our modeling also predicts that the tank-treading period GP_{tt} increases linearly with the ratio of the cytoplasm viscosity to that of the suspending medium. This dependence is consistent with the increased hydrodynamic forces in the cytoplasm, which slow down the rotation of the inner fluid and thus the erythrocyte membrane. Our findings provide insight on the effects of the paraproteinemia, i.e., a family of disorders associated with elevated plasma protein levels and thus higher plasma viscosity (16).

Our cytoskeleton-based modeling also provides insight on the local surface area changes of the spectrin skeleton during the tank-treading of the cells, and thus complements the earlier work of Fischer (26) and Discher et al. (31). In particular, our work shows that during tank-treading, the cytoskeleton undergoes measurable local area dilatation and compression, as also found experimentally via micropipette experiments at large static deformations (31).

The senior author of this article (P.D.) thanks Dr. Fischer for providing the experimental data from his recent study (2). Most computations were performed on multiprocessor computers provided by the National Center for Supercomputing Applications in Illinois.

This work was supported in part by the National Science Foundation grant No. CBET0730033 and the National Institutes of Health grant No. R03EB006800.

REFERENCES

1. Fischer, T. M., M. Stöhr-Liesen, and H. Schmid-Schönbein. 1978. The red cell as a fluid droplet: tank tread-like motion of the human erythrocyte membrane in shear flow. *Science.* 202:894–896.
2. Fischer, T. M. 2007. Tank-tread frequency of the red cell membrane: dependence on the viscosity of the suspending medium. *Biophys. J.* 93:2553–2581.
3. Abkarian, M., M. Faivre, and A. Viallat. 2007. Swinging of red blood cells under shear flow. *Phys. Rev. Lett.* 98:188302.
4. Pozrikidis, C. 2003. Numerical simulation of the flow-induced deformation of red blood cells. *Ann. Biomed. Eng.* 31:1194–1205.
5. Sui, Y., Y. T. Chew, …, H. T. Low. 2008. Dynamic motion of red blood cells in simple shear flow. *Phys. Fluids.* 20:112106.
6. Keller, S. R., and R. Skalak. 1982. Motion of a tank-treading ellipsoidal particle in a shear flow. *J. Fluid Mech.* 120:27–47.
7. Skotheim, J. M., and T. W. Secomb. 2007. Red blood cells and other nonspherical capsules in shear flow: oscillatory dynamics and the tank-treading-to-tumbling transition. *Phys. Rev. Lett.* 98:078301.
8. Boey, S. K., D. H. Boal, and D. E. Discher. 1998. Simulations of the erythrocyte cytoskeleton at large deformation. I. Microscopic models. *Biophys. J.* 75:1573–1583.
9. Discher, D. E., D. H. Boal, and S. K. Boey. 1998. Simulations of the erythrocyte cytoskeleton at large deformation. II. Micropipette aspiration. *Biophys. J.* 75:1584–1597.
10. Li, J., M. Dao, …, S. Suresh. 2005. Spectrin-level modeling of the cytoskeleton and optical tweezers stretching of the erythrocyte. *Biophys. J.* 88:3707–3719.
11. Fedosov, D. A., B. Caswell, and G. E. Karniadakis. 2010. A multiscale red blood cell model with accurate mechanics, rheology, and dynamics. *Biophys. J.* 98:2215–2225.
12. Hardemann, M. R., P. T. Goedhart, …, K. P. Lettinga. 1994. Laser-assisted optical rotational cell analyzer (LORCA): I. A new instrument for measurement of various structural hemorheological parameters. *Clin. Hem.* 14:605–618.
13. Skalak, R., N. Özkaya, and T. C. Skalak. 1989. Biofluid mechanics. *Annu. Rev. Fluid Mech.* 21:167–204.
14. Mohandas, N., and J. A. Chasis. 1993. Red blood cell deformability, membrane material properties and shape: regulation by transmembrane, skeletal and cytosolic proteins and lipids. *Sem. Hem.* 30:171–192.
15. Evans, E., and Y.-C. Fung. 1972. Improved measurements of the erythrocyte geometry. *Microvasc. Res.* 4:335–347.
16. Baskurt, O. K., and H. J. Meiselman. 2003. Blood rheology and hemodynamics. *Sem. Thromb. Hem.* 29:435–450.
17. Fischer, T. M. 2004. Shape memory of human red blood cells. *Biophys. J.* 86:3304–3313.
18. Dodson, III, W. R., and P. Dimitrakopoulos. 2009. Dynamics of strain-hardening and strain-softening capsules in strong planar extensional flows via an interfacial spectral boundary element algorithm for elastic membranes. *J. Fluid Mech.* 641:263–296.
19. Pozrikidis, C., editor. 2003. Modeling and Simulation of Capsules and Biological Cells. Chapman and Hall/CRC, Boca Raton, FL.
20. Dodson, III, W. R., and P. Dimitrakopoulos. 2008. Spindles, cusps and bifurcation for capsules in Stokes flow. *Phys. Rev. Lett.* 101: 208102.
21. Skalak, R., A. Tozeren, …, S. Chien. 1973. Strain energy function of red blood cell membranes. *Biophys. J.* 13:245–264.
22. Hénon, S., G. Lenormand, …, F. Gallet. 1999. A new determination of the shear modulus of the human erythrocyte membrane using optical tweezers. *Biophys. J.* 76:1145–1151.
23. Secomb, T. W., R. Hsu, and A. R. Pries. 2002. Blood flow and red blood cell deformation in nonuniform capillaries: effects of the endothelial surface layer. *Microcirculation.* 9:189–196.
24. Fischer, T. M. 1980. On the energy dissipation in a tank-treading human red blood cell. *Biophys. J.* 32:863–868.
25. Hochmuth, R. M., P. R. Worthy, and E. A. Evans. 1979. Red cell extensional recovery and the determination of membrane viscosity. *Biophys. J.* 26:101–114.
26. Fischer, T. M. 1992. Is the surface area of the red cell membrane skeleton locally conserved? *Biophys. J.* 61:298–305.
27. Sukumaran, S., and U. Seifert. 2001. Influence of shear flow on vesicles near a wall: a numerical study. *Phys. Rev. E Stat. Nonlin. Soft Matter Phys.* 64:011916.
28. Lac, E., and D. Barthès-Biesel. 2005. Deformation of a capsule in simple shear flow: effect of membrane prestress. *Phys. Fluids.* 17:072105.

29. Åström, K. J., and T. Hägglund. 1995. PID Controllers: Theory, Design, and Tuning. International Society for Measurement and Control, Research Triangle Park, NC.
30. Lenormand, G., S. Hénon, …, F. Gallet. 2001. Direct measurement of the area expansion and shear moduli of the human red blood cell membrane skeleton. *Biophys. J.* 81:43–56.
31. Discher, D. E., N. Mohandas, and E. A. Evans. 1994. Molecular maps of red cell deformation: hidden elasticity and in situ connectivity. *Science.* 266:1032–1035.
32. Stamenović, D., N. Wang, and D. E. Ingber. 2006. Cellular tensegrity models and cell-substrate interactions. *In* Principles of Cellular Engineering: Understanding the Biomolecular Interface. M. R. King, editor. Academic Press, London, UK.